OPEN ACCESS

ACTA METALLURGICA SLOVACA

2025, VOL. 31, NO. 4, 238-252

SCICELL

RESEARCH PAPER

Research into the possibility of extracting nickel and cobalt from pyrite tailings using a combined method

Kulzira Mamyrbayeva[1], Almira Kuandykova[1], Tatyana Chepushtanova[1], Yerik Merkibayev[1], Brajendra Mishra[2], Ainur Sultanbayeva.[1]*

[1] Department of Metallurgy and Mineral Processing, Satbayev University, 22a Satpaev Str., Almaty, 050013, Kazakhstan
[2] Mechanical & Materials Engineering Department; Worcester Polytechnic Institute, Worcester, MA | 01609-2280, USA
*Corresponding author: a.kuandykova@satbayev.university, Department of Metallurgy and Mineral Processing, Satbayev University, 22a Satpaev Str., Almaty, 050013, Kazakhstan

Received: 27.09.2025
Accepted: 31.10.2025

ABSTRACT

Due to the sharp increase in demand and prices for nickel and cobalt, the search for new sources of raw materials has become a pressing issue. This study presents a comprehensive thermodynamic and kinetic analysis of the combined method of oxygen-deficient oxidative roasting and subsequent acid leaching to extract nickel and cobalt from pyrite waste sourced from Kazakhstani enterprises. The thermodynamic analysis showed that, under oxygen deficiency, thermal decomposition of higher sulfides forms non-stoichiometric, soluble lower sulfides of iron, nickel, and cobalt. The kinetic study revealed that the process is complex and multi-stage, and that it proceeds at a high rate in the 610–680 °C range, where kinetic factors control it. Activation energies were calculated for three stages: 105–115 kJ/mol for Stage I (450–479.3 °C), 310–320 kJ/mol for Stage II (661.8 °C), and 390–420 kJ/mol for Stage III (749.7–789 °C). Experimental studies confirmed the effectiveness of roasting at 700 °C for 60 minutes. Subsequent sulfuric acid leaching of the obtained sinders under optimal conditions (sulfuric acid excess coefficient R of 1.5 times the stoichiometric amount, temperature of 100 °C, and a duration of 2 hours) yielded high metal recoveries: 94.5% Fe, 93.4% Ni, and 91% Co. The developed technology, combining thermal activation and leaching, proved effective and is recommended for processing similar raw materials.

Keywords: pyrite concentrate, nickel, cobalt, thermodynamic analysis, decomposition of pyrite concentrate

INTRODUCTION

Pyrite tailings are a by-product of the processing of sulphide ores, mainly composed of pyrite (FeS_2). In addition to the main component, they often contain minerals of several important non-ferrous metals (Co, Ni, Cu, etc.) that can be used in green energy technologies. These include minerals such as pentlandite ($(Fe,Ni)_9S_8$), chalcopyrite ($CuFeS_2$), pyrrhotite ($Fe_{1-x}S$), and various cobalt sulphides [1-2].

The market for processing mining waste in Kazakhstan is largely undeveloped, particularly for extracting nickel and cobalt from tailings and intermediate products of operating enterprises. Meanwhile, global prices and demand for nickel and cobalt are increasing annually, driven by demand for nickel–cobalt batteries for electric vehicles, special alloys, and other products.

The pyrite concentrate from the Sokolovsko-Sarbaisky Mining and Processing Production Association (SSGPO) represents a valuable technogenic resource. Although the Ni and Co content in these tailings is relatively low, their total reserves are potentially significant.

Processing such raw materials not only reduces waste volume and frees up land, but also prevents soil and water pollution by heavy metals (acid mine drainage, AMD) [3-4]; and allows the extraction of additional materials such as iron, nickel, cobalt, copper, and sulphur (in the form of sulphur dioxide for sulphuric acid production).

Given the sharp increase in demand for nickel and cobalt, pyrite tailings can be considered an important resource for their extraction. Methods for extracting Ni and Co from pyrite tailings can be divided into several categories: pyrometallurgical, hydrometallurgical, and combined methods.

Pyrometallurgical processes (e.g., roasting followed by smelting) can be used but are less common due to the low nickel and cobalt concentrations and the high sulphur and iron content, which lead to high energy consumption and large volumes of waste gases.

However, roasting can be used to prepare material for hydrometallurgical processing—for example, to oxidise sulphides and increase their solubility. Hydrometallurgical processing of pyrite tailings is the most promising due to its flexibility and environmental friendliness. Leaching of tailings is the main stage of hydrometallurgical processing.

Acid leaching using sulphuric as sulfuric (H_2SO_4) [5-7], hydrochloric (HCl) [8-9], or nitric (HNO_3) acids [10-12], as well as mixed reagent leaching [13-14] and autoclave leaching with various oxidants [15-16] are employed. Pressure leaching (autoclave leaching) enables high metal extraction by raising temperature and pressure, thereby accelerating reactions. Alongside chemical leaching, bioleaching of nickel and cobalt - using microorganisms (e.g., Acidithiobacillus ferrooxidans) to oxidise sulphides - promotes metal dissolution. This method is environmentally friendly but has a long cycle and requires careful control of conditions in harsh continental climates [17-21].

The leaching behaviour of sulphidic pyrite concentrate depends largely on the specific minerals present; even similar minerals can differ in solubility across deposits. Sulphuric acid leaching is one of the most common methods for extracting nickel and cobalt, as it is used to process copper–nickel intermediates (fines or mattes). This method is versatile and fast, and provides complete metal extraction with selective dissolution of impurities. In addition, it allows full utilisation of all components of the raw material, including iron and sulphur, to produce commercial products.

One of the most effective methods for processing Ni–Co-bearing pyritic raw materials is a combined technology, including the roasting of sulphide materials followed by leaching [22-28]. Depending on the tailing's composition, either sulphidation roasting (limited oxygen supply) or oxidation roasting (with air flow) is carried out. Under limited oxygen conditions during roasting, in addition to forming soluble metal sulphides, sulphurous gases are produced from sulphur oxidation; these gases are valuable for sulphuric acid production. If the roasting conditions favor the dissociation of pyrite, the formation of S_2 gas is possible. Advantages of roasting pyrite tailings in an oxygen-limited environment include control over sulphur release (obtaining sulphur as SO_2 for acid production or as elemental sulphur) and the formation of more soluble, reactive iron compounds (lower iron sulphides) that dissolve more readily in acids than the original pyrite. This approach enables the simultaneous extraction of nickel, cobalt, and iron from tailings, establishing a closed-loop process. Sulphuric acid is a promising leaching agent.

This research aimed to study the extraction of nickel, cobalt, and iron from nickel-cobalt-bearing pyrite concentrate using a combined "thermal activation - acid leaching" technology. In particular, the work involved a thermodynamic analysis of the sulfidation roasting process under oxygen-deficient conditions and subsequent sulphuric acid leaching of the calcine.

MATERIAL AND METHODS

Methods of analysis

The material studied was nickel–cobalt-bearing pyrite tailings from the magnetic separation of sulphide–magnetite ores at the Sokolovsko-Sarbaisky Mining and Processing Production Association (SSGPO), Kazakhstan.

For the qualitative and quantitative analysis of the initial solid samples and solutions, chemical, atomic-emission, and X-ray phase analysis methods were employed, and EDS was used to examine the particle surface microstructure.
X-ray phase analysis of the initial and heat-treated samples was performed on a D8 Advance diffractometer (BRUKER) using the powder method with filtered Cu or Co radiation at 40 kV and 30 mA.
Diffractogram data processing and interplanar distance calculations were performed using EVA software. Phase identification and searching were performed using the Search/match program with the PDF-2 Powder Diffractometry Database.
The microstructure of the samples was examined using a JEOL JSM-6490LA SEM equipped with an integrated energy-dispersive X-ray analyzer (EDS). This setup enables seamless EDS data collection and analysis. The microscope has a high resolution of 3.0 nm, a take-off angle of 35°, and an analytical working distance of 10 mm. Thermodynamics of key reactions involved in the sulfidation process, equilibrium phase diagrams for Fe–S–O, Ni-S-O Co-S-O systems during heat treatment of the systems were performed using a NETZSCH STA 409 PC/PG thermal analysis instrument in an inert atmosphere: the analysis combined differential thermogravimetry (DTG) and differential scanning calorimetry (DSC). The thermal decomposition of the ore was studied over a temperature range of 0–1000°C. To determine the metal content in the samples, a Shimadzu AA-7000 atomic absorption spectrometer from Japan was used. The analysis followed standard atomic absorption spectroscopy methods using an acetylene/air flame. The instrument was calibrated with standard solutions of the corresponding elements.

Roasting and leaching methods

Experiments on roasting the pyrite concentrate were conducted in a fluidised-bed furnace with an oxygen-enriched air blast (15% O_2) at 600–700 °C for 1 hour.
Sulphuric acid solution was used for leaching. Leaching was carried out in a 0.5 L glass reactor equipped with a paddle stirrer and a reflux condenser, placed in a thermostat that maintained the temperature within ± 0.2 °C of the setpoint **(Fig. 1).**

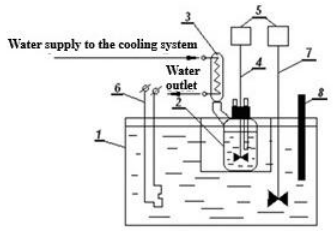

1 – thermostat;
2 – leaching reactor;
3 – reflux condenser;
4 – solution agitator;
5 – electric motor;
6 – heater;
7 – coolant agitator;
8 – mercury contact thermometer

Fig. **1** Schematic diagram of the leaching apparatus

The sample, sealed in a glass ampoule, was placed in the reactor containing acid. Once the set temperature was reached, the stirrer was activated; its rotation broke the ampoule containing the sample, marking the start of leaching. The thermostat used circulating glycerine as the heat-transfer fluid. The pH of the solution and the concentrations of iron, nickel, and cobalt were monitored during leaching. Leaching experiments were conducted over a temperature range of 20–110 °C, using 50 g of pyrite concentrate per test. Leaching time varied from 30 to 300 minutes, and the acid amount was 0.5–2.5 times the stoichiometric requirement for complete metal dissolution.

RESULTS AND DISCUSSION

Raw materials and reagents

Nickel–cobalt-bearing tailings obtained from the magnetic separation stage at SSGPO (from sulphide–magnetite ore processing), hereinafter referred to as the pyrite concentrate, were used as the starting material. The chemical composition is shown in **Table 1**.
The following phases were identified in the studied concentrate via semi-quantitative X-ray phase analysis (**Table 2**).
Semi-quantitative XRD phase analysis was performed to identify the mineral phases present in the concentrate. The results show that the material is a complex mixture of sulphides and gangue minerals. The main sulphide mineral is pyrite (FeS_2), which accounts for ~17.6% of the sample. No discrete Ni or Co sulphide minerals were detected by XRD, presumably because their concentrations are below the detection limit; instead, Ni and Co are likely present within the lattice of iron sulphides (e.g. substituting in pentlandite or pyrite). The bulk of the tailings is composed of silicate and aluminosilicate gangue: analcime (~25%), albite (~9%), tremolite (~9%), and others. Notably, magnetite (Fe_3O_4) is present (~6.3%), indicating some iron was oxidised during the original ore processing. Calcium-containing minerals such as calcite ($CaCO_3$, ~6.9%) and dolomite ($CaMg(CO_3)_2$, ~4.6%) are also present, along with minor potassium feldspar, chlorite, and mica. The gangue composition correlates with the high SiO_2, Al_2O_3, and CaO content seen in.

Table 1 Chemical composition of the pyrite concentrate

Content, %						
Fe	**Cu**	**Co**	**Ni**	**S**	**Pb**	**Zn**
15,78	0,03	0,013	0,012	4,50	0,022	0,040
SiO_2	**Al_2O_3**	**CaO**	**MgO**	**TiO_2**	**As**	
34,63	12,97	11,32	3,55	0,64	0,008	

Table 2 Results of semi-quantitative X-ray phase analysis

Phase name	**Formula**	**Concentration, %**
Analcime	$Na[AlSi_2O_6](H_2O)$	25,0
Pyrite	FeS_2	17,6
Albite	$(Na,Ca)Al(Si,Al)_3O_8$	9,4
Tremolite	$(Ca, Na, Fe)_2Mg_5Si_8O_{22}(OH)_2$	9,1
Calcite	$Ca(CO_3)$	6,9
Grossular, OH-rich	$Ca_3Al_2(SiO_4)_2(OH)_4$	6,8
Magnetite	Fe_3O_4	6,3
Quartz	SiO_2	4,8
Dolomite	$CaMg(CO_3)_2$	4,6
Potassium Feldspar	$KAlSi_3O_8$	3,9
Chlorite	$Mg,Fe)_5Al(Si_3Al)O_{10}(OH)_8$	3,1
Mica	$KAl_2(AlSi_3O_{10})(OH)_2$	2,5

Under reflected-light microscopy, the sulphide minerals in the tailings were observed in a multiphase assemblage. In addition to abundant magnetite, pyrite, and minor hematite, other sulphides such as sphalerite (ZnS), chalcopyrite ($CuFeS_2$), and pyrrhotite ($Fe_{1-x}S$) were identified; their presence was confirmed by microprobe (EDS) analysis. Discrete nickel and cobalt sulphide phases were not observed under the microscope or detected by XRD, implying that Ni and Co are finely disseminated or in solid solution within other sulphides. According to bulk chemical analysis, the tailings contain ~15.78% Fe and ~5.5% S, but only 0.012–0.013% Ni and Co each. Nickel and cobalt in these tailings are most likely associated with iron sulphides (e.g., pentlandite inclusions in pyrite/pentlandite intergrowths). In such a form, Ni and Co are difficult to extract by direct leaching, as they are locked within the sulphide matrix. **Fig. 2** shows an XRD diffractogram of the raw pyrite tailings, highlighting the peaks of pyrite and major gangue minerals.

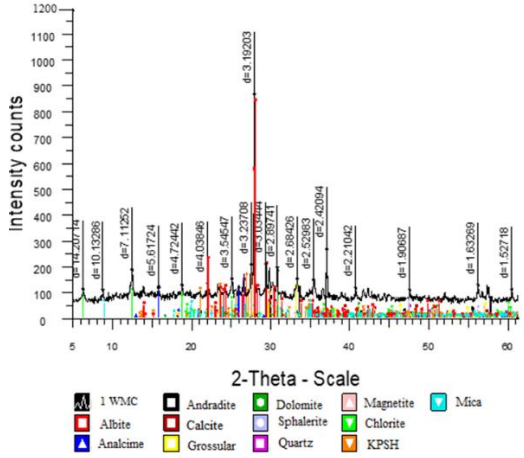

Fig. 2 Diffractogram of pyrite concentrate

Nickel and cobalt in the tailings thus occur in intimate association with iron sulphides (pyrite, pyrrhotite) and copper–iron sulphide (chalcopyrite). These Ni–Co-bearing sulphides are intergrown with the iron sulphide crystals, making conventional direct extraction challenging.

Thermal activation (roasting) was therefore proposed to convert these sulphides into more leachable compounds. In this study, we focus on roasting under limited oxygen (α=30-50%) to produce lower sulphides, followed by sulphuric acid leaching of the roasted product.

For this purpose, a comprehensive thermodynamic analysis was carried out, and the decomposition kinetics were studied.

Calculation of thermodynamic parameters of sulphide decomposition reactions

Thermodynamic calculations were performed to predict the behaviour of the main sulphide components during roasting of the pyrite concentrate under oxygen-limited conditions. The calculations were carried out using the HSC Chemistry 10 software for the 500–1000 °C range, assuming a low oxygen partial pressure. Under such oxygen-deficient conditions, the sulphides of iron, nickel, and cobalt are expected to oxidise only partially. In essence, higher sulphides should decompose to form lower sulphides (with less sulphur) and sulfur dioxide.

Table 3 summarises the standard thermodynamic parameters (enthalpy ΔH, entropy ΔS, Gibbs free energy ΔG, and equilibrium constant K) for several main reactions representing the oxidation of iron sulphides under limited oxygen supply. **Table 4** similarly presents the data for cobalt- and nickel-sulphide oxidation reactions.

Table 3 Thermodynamic parameters of main oxidation reactions of iron sulphides (oxygen-limited conditions)

№	Reaction	T (°C)	ΔH (kJ/mol)	ΔS (J/mol·K)	ΔG (kJ/mol)	K	logK
1	$7Fe_2S_3 + 5/7O_2 = 2Fe_7S_8 + 5SO_2$	500	-752,341	712,789	-1303,434	1,171E+088	88,068
		600	-691,118	787,249	-1378,505	2,975E+082	82,474
		700	-629,124	854,461	-1460,643	2,558E+078	78,408
		800	-566,172	916,029	-1549,209	2,587E+075	75,413
		900	-502,163	973,051	-1643,697	1,556E+073	73,192
		1000	-437,053	1026,306	-1743,694	3,516E+071	71,546
2	$Fe_7S_8 + O_2 = 7FeS + SO_2$	500	-182,060	132,978	-284,873	1,769E+019	19,248
		600	-181,552	133,603	-298,207	6,938E+017	17,841
		700	-181,298	133,879	-311,582	5,319E+016	16,726
		800	-180,752	134,408	-324,992	6,607E+015	15,820
		900	-179,311	135,683	-338,488	1,182E+015	15,072
		1000	-176,334	138,109	-352,167	2,818E+014	14,450
3	$FeS_2 + O_2 = FeS + SO_2$	500	-215,629	77,029	-275,184	3,919E+018	18,593
		600	-215,601	77,065	-282,890	8,410E+016	16,925
		700	-215,654	77,007	-290,594	3,974E+015	15,599
		800	-215,695	76,967	-298,292	3,314E+014	14,520
		900	-215,625	77,028	-305,991	4,221E+013	13,625
		1000	-215,349	77,252	-313,703	7,442E+012	12,872
4	$FeS_2 + 6/7O_2 = 1/7Fe_7S_8 + 6/7SO_2$	500	-189,620	58,032	-234,488	6,975E+015	15,844
		600	-189,665	57,979	-240,289	2,377E+014	14,376
		700	-189,755	57,882	-246,082	1,621E+013	13,210
		800	-189,873	57,766	-251,865	1,821E+012	12,260
		900	-190,010	57,645	-257,635	2,966E+011	11,472
		1000	-190,159	57,523	-263,394	6,418E+010	10,807
5	$FeS_2 + 0,86O_2 = 1,14\ Fe_{0,877}S + 0,86\ SO_2$	500	-175,072	53,994	-216,817	4,463E+014	14,650
		600	-175,059	54,012	-222,220	1,972E+013	13,295
		700	-175,206	53,854	-227,614	1,654E+012	12,218
		800	-175,409	53,654	-232,988	2,195E+011	11,341
		900	-175,361	53,695	-238,353	4,108E+010	10,614
		1000	-175,034	53,961	-243,734	1,002E+010	10,001
6	$FeS_2 + 1/2O_2 = 1/2Fe_2S_3 + 1/2SO_2$	500	-135,882	7,119	-141,386	3,572E+009	9,553
		600	-140,299	1,747	-141,824	3,056E+008	8,485
		700	-144,817	-3,151	-141,751	4,067E+007	7,609
		800	-149,432	-7,664	-141,207	7,477E+006	6,874
		900	-154,141	-11,859	-140,228	1,755E+006	6,244
		1000	-158,941	-15,785	-138,844	4,977E+005	5,697
7	$0,877Fe_2S_3 + 0,631O_2 = 2Fe_{0,877}S + 0,631\ SO_2$	6500	-111,807	95,503	-185,645	3,494E+012	12,543
		600	-104,033	104,961	-195,679	5,095E+011	11,707
		700	-96,402	113,236	-206,598	1,231E+011	11,090
		800	-88,714	120,752	-218,299	4,231E+010	10,626
		900	-80,360	128,190	-230,746	1,883E+010	10,275
		1000	-71,286	135,608	-243,936	1,021E+010	10,009
8	$Fe_{0,877}S + 0,123O_2 = 0,877FeS + 0,123SO_2$	500	-14,035	13,560	-24,519	4,536E+001	1,657
		600	-14,023	13,574	-25,875	3,532E+001	1,548
		700	-13,923	13,681	-27,237	2,898E+001	1,462
		800	-13,755	13,846	-28,614	2,471E+001	1,393
		900	-13,742	13,859	-30,000	2,167E+001	1,336
		1000	-13,827	13,790	-31,383	1,940E+001	1,288

Comparing the thermodynamic parameters of reactions (**1**)–(**8**) for iron sulphide oxidation at 500–1000 °C shows that reaction (**1**) is the most thermodynamically favorable. This reaction has the most negative ΔG values (from –1303.434 to –1743.694 kJ/mol) and very high equilibrium constants (log K from 88.068 to 71.546). Next in thermodynamic favorability are reactions (**2**) and (**3**), which represent the complete conversion of Fe_7S_8 (reaction **2**) to pyrrhotite (FeS). Reaction (**3**) is characterized by relatively low ΔG values (from –284.873 to –352.167 kJ/mol) and extremely high log K values (from 19.248 to 12.872) in the 500–1000 °C range, confirming its high probability. The next most probable reactions are (**4**) and (**5**), which describe the formation of iron sulphides with disproportionate sulphur content. Reaction (**5**) becomes thermodynamically favorable already at 500 °C, with ΔG from –275.184 to –313.703 kJ/mol. Its log K is $3.919 \cdot 10^{18}$ at 500 °C and decreases to $7.44 \cdot 10^{12}$ at 1000 °C, demonstrating the high efficiency of direct oxidation of pyrite to iron monosulphide.

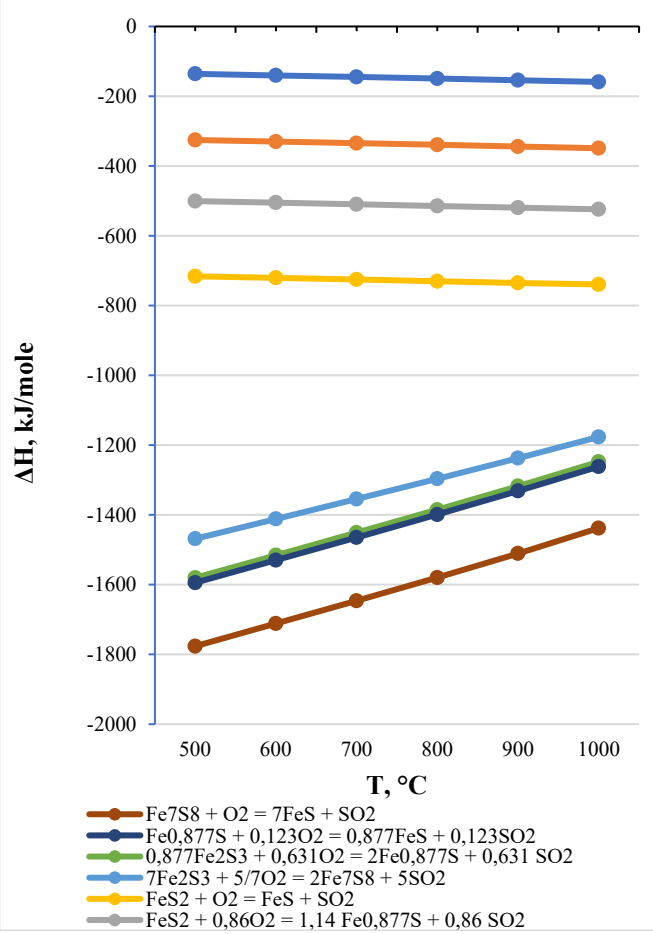

Fig. 3 Temperature dependence of ΔH for the oxidation reactions of iron sulphides in the 500–1000°C range

Based on these data, it can be concluded that for most reactions an increase in temperature is favorable, as the ΔG values become more negative. All the reactions are exothermic, as their ΔH values are negative (see Fig. 3), and they are accompanied by an increase in entropy (ΔS > 0). The least likely reaction is (**8**), which has the smallest negative ΔG values (–24.519 to –31.383 kJ/mol). For reactions (**2**), (**8**), (**7**), and (**1**), raising the temperature from 500 to 1000 °C decreases ΔH (**Fig. 3**), indicating an increase in the exothermicity of these oxidation processes. For reactions (**3**), (**4**), (**5**), and (**6**), by contrast, increasing the temperature is unfavorable, as the amount of heat released decreases.

The log K versus T diagram (**Fig. 4**) shows that, for all reactions, increasing temperature decreases log K, indicating that the equilibrium shifts toward product formation.

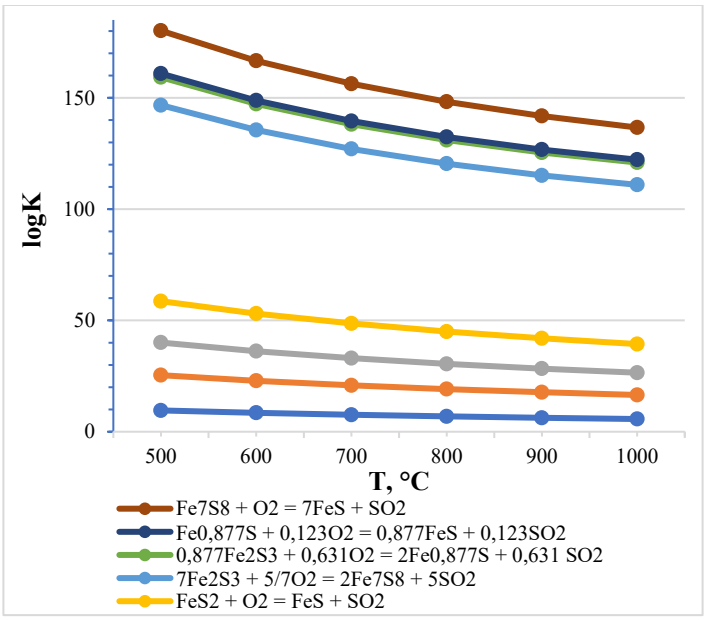

Fig. 4 Temperature dependence of log K for the oxidation reactions of iron sulphides in the 500–1000 °C range

Analysis of the thermodynamic data for cobalt and nickel sulphide oxidation indicates that the oxidation of nickel sulphides is more thermodynamically probable than that of cobalt sulphides (see **Table 4**).

Reactions (**15**), (**14**), and (**17**) have more negative ΔG values (500–1000 °C) compared to the cobalt sulphide reactions (**9–13**), indicating their higher thermodynamic probability.

Oxidation of the sulphides under oxygen-limited conditions occurs in stages, with sulphides progressing from more “sulphur-rich” to less “sulphur-rich” forms until the final product with the lowest sulphur content is formed. In the Ni–S–O and Co–S–O systems, a similar multi-stage oxidation sequence is observed, ultimately yielding lower-sulphur phases as temperature increases.

Table 4 Thermodynamic parameters of the main oxidation reactions of cobalt and nickel sulphides involved in the thermal activation process

№	Reaction	T (°C)	ΔH (kJ/mol)	ΔS (J/mol·K)	ΔG (kJ/mol)	K	logK
9	$CoS_2 + O_2 = CoS + SO_2$	500	-246,691	20,310	-262,393	5,358E+017	17,729
		600	-247,092	19,822	-264,399	6,585E+015	15,819
		700	-247,509	19,370	-266,359	1,987E+014	14,298
		800	-247,953	18,936	-268,274	1,146E+013	13,059
		900	-248,431	18,510	-270,146	1,070E+012	12,029
		1000	-248,946	18,089	-271,976	1,444E+011	11,160
10	$CoS_2 + 0.555O_2 = CoS_{0,89} + 1,11SO_2$	500	58,055	102,827	-21,446	2,812E+001	1,449
		600	57,267	101,869	-31,680	7,858E+001	1,895
		700	56,443	100,975	-41,821	1,758E+002	2,245
		800	55,583	100,135	-51,876	3,352E+002	2,525
		900	54,690	99,339	-61,850	5,677E+002	2,754
		1000	53,764	98,582	-71,746	8,786E+002	2,944
11	$3CoS_{1,333} + O_2 = 3\ CoS + SO_2$	500	-428,396	-260,347	-227,108	2,213E+015	15,345
		600	-497,383	-344,150	-196,888	6,018E+011	11,779
		700	-575,224	-428,467	-158,261	3,130E+008	8,496
		800	-661,942	-513,220	-111,180	2,583E+005	5,412
		900	-757,551	-598,343	-55,605	2,992E+002	2,476
		1000	-862,060	-683,783	8,499	4,480E-001	-0,349
12	$CoS_{1,333} + 0,443O_2 = CoS_{0,89} + 0,443SO_2$	500	-194,493	-122,120	-100,076	5,778E+006	6,762
		600	-225,127	-159,334	-86,005	1,398E+005	5,146
		700	-259,635	-196,713	-68,204	4,583E+003	3,661
		800	-298,024	-234,232	-46,657	1,867E+002	2,271
		900	-340,302	-271,874	-21,353	8,930E+000	0,951
		1000	-386,474	-309,621	7,721	4,822E-001	-0,317
13	$CoS + 0,11O2 = CoS_{0,89} + 0,11SO_2$	500	-30,658	-3,993	-27,571	7,292E+001	1,863
		600	-30,885	-4,269	-27,157	4,215E+001	1,625
		700	-31,095	-4,497	-26,719	2,718E+001	1,434
		800	-31,288	-4,686	-26,259	1,898E+001	1,278
		900	-31,465	-4,844	-25,782	1,406E+001	1,148
		1000	-31,628	-4,977	-25,291	1,091E+001	1,038
14	$3NiS_2 + 2O_2 = Ni_3S_4 + 2SO_2$	500	-498,661	56,752	-542,539	4,544E+036	36,657
		600	-495,131	61,035	-548,423	6,474E+032	32,811
		700	-490,696	65,834	-554,763	6,024E+029	29,780
		800	-485,381	71,026	-561,603	2,177E+027	27,338
		900	-479,199	76,529	-568,978	2,168E+025	25,336
		1000	-472,155	82,285	-576,917	4,696E+023	23,672
15	$3NiS_2 + 4O_2 = Ni_3S_2 + 4SO_2$	500	-1022,269	61,256	-1069,629	1,867E+072	72,271
		600	-965,818	129,287	-1078,705	3,444E+064	64,537
		700	-963,928	131,341	-1091,743	4,029E+058	58,605
		800	-942,744	151,342	-1105,156	6,267E+053	53,797
		900	-941,542	152,416	-1120,349	7,725E+049	49,888
		1000	-940,869	152,970	-1135,622	3,946E+046	46,596
16	$Ni_3S_4 + O_2 = 3NiS + SO_2$	500	-269,603	24,781	-288,762	3,241E+019	19,511
		600	-274,226	19,163	-290,959	2,556E+017	17,408
		700	-279,386	13,574	-292,595	5,089E+015	15,707
		800	-285,095	7,994	-293,674	1,975E+014	14,296
		900	-291,358	2,418	-294,194	1,259E+013	13,100
		1000	-207,843	69,173	-295,911	1,386E+012	12,142
17	$Ni_3S_4 + 2O_2 = Ni_3S_2 + 2SO_2$	500	-523,608	4,504	-527,090	4,108E+035	35,614
		600	-470,687	68,253	-530,282	5,319E+031	31,726
		700	-473,232	65,507	-536,980	6,688E+028	28,825
		800	-457,363	80,315	-543,553	2,879E+026	26,459
		900	-462,343	75,888	-551,371	3,564E+024	24,552
		1000	-468,714	70,684	-558,705	8,403E+022	22,924
18	$3NiS + O_2 = SO_2 + Ni_3S_2$	500	-254,005	-20,277	-238,329	1,268E+016	16,103
		600	-196,461	49,089	-239,324	2,081E+014	14,318
		700	-193,846	51,933	-244,385	1,314E+013	13,119
		800	-172,268	72,321	-249,880	1,458E+012	12,164
		900	-170,986	73,469	-257,176	2,830E+011	11,452
		1000	-260,870	1,511	-262,794	6,065E+010	10,783

The increase in temperature is favorable only for the reaction **(10)**. For the other reactions, as the temperature rises, the equilibrium constants shift to the left, i.e., towards the starting substances, indicating an increase in the difficulty of the oxidation reactions (**Fig. 5**).

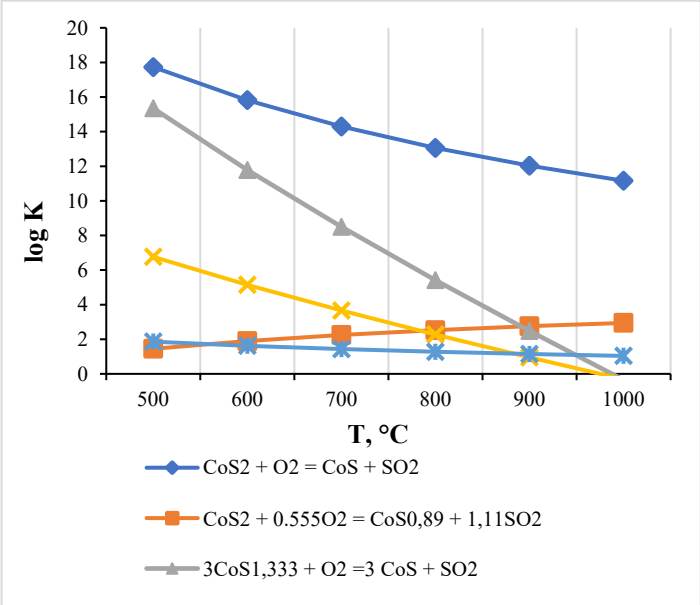

Fig. 5 Dependence of log K on T for the oxidation reactions of cobalt sulphides

The diagram (**Fig. 6**) showing the dependence of ΔH on temperature for reactions involving cobalt sulphides in the range 500-1000°C shows that, except for reaction (10), which is endothermic (ΔH> 0), all other reactions are exothermic. The most exothermic reaction is reaction (10); its enthalpy ΔH becomes more negative (increases in magnitude) by almost 2 times, changing from -428.368 to -862.06. kJ/mol. The second- and third-most exothermic reactions are **(9)** and **(12)**. In the reaction **(12)**, ΔH also becomes twice as negative (from -194.493 to -386.474 kJ/mol). The value of ΔH for reaction (**13**) is not very temperature-dependent, changing over this interval from -30.658 to -31.628 kJ/mol.

Thus, based on the calculation of ΔH for the oxidation reactions of cobalt sulphides, it can be concluded that the most energetically favourable reaction is the formation of cobalt monosulphide, since it has the highest negative enthalpy values (ΔH). The other oxidation reactions are less favourable or, in the case of endothermic reactions, are hindered by an increase in temperature.

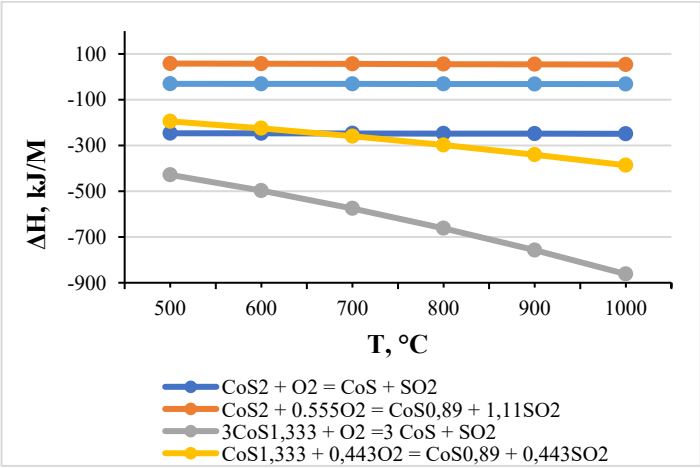

Fig. 6 Temperature dependence of ΔH for cobalt sulphide oxidation reactions in an oxygen-limited atmosphere

Analysis of the ΔlogK versus temperature (T) diagram (**Fig. 7**) for nickel sulphide oxidation reactions shows that across the entire temperature range of 500-1000 °C, all reactions proceed towards the formation of products - lower sulphides. At the same time, since all these reactions are exothermic, logK values decrease with increasing temperature, which indicates a shift in equilibrium towards the starting materials as the temperature rises.

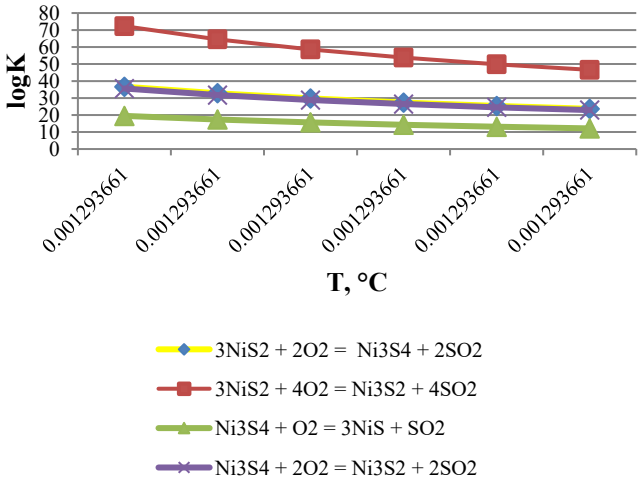

Fig. 7 Δlog K vs. T for nickel sulphide oxidation reactions in an oxygen-limited atmosphere

The ΔH vs. T diagram for nickel sulphide oxidation reactions (**Fig. 8**) shows that the reactions are exothermic (ΔH < 0). In terms of enthalpy, reaction (15) is the most exothermic. As temperature rises, its enthalpy becomes less negative (from –1022.269 to –940.869 kJ/mol).

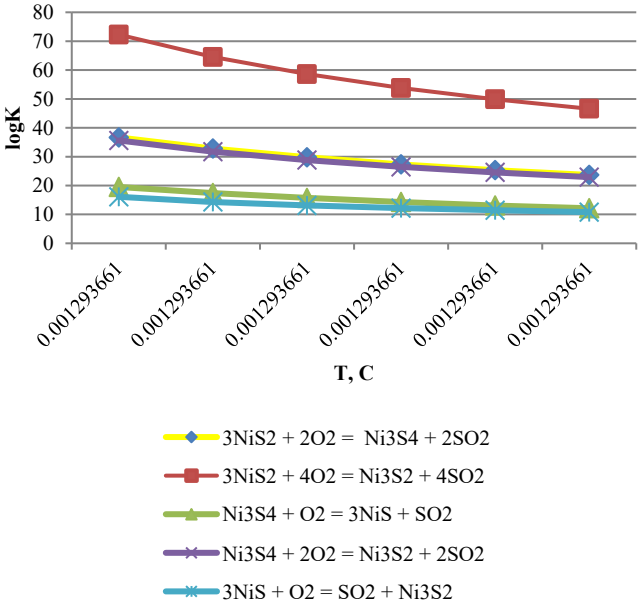

Fig. 8 Temperature dependence of ΔH for nickel sulphide oxidation reactions in an oxygen-limited atmosphere

Reactions (14) and (17) are moderately exothermic, while reactions (16) and (18) are the least exothermic. However, reaction (16) demonstrates an interesting feature: as the temperature increases from 500 to 900°C, its enthalpy decreases in magnitude, but then, starting at 900°C, it becomes more negative. This is due to

the difficulty of this reaction at high temperatures and to the tendency of the resulting NiS to melt, an endothermic process. This is due to the difficulty of this reaction at high temperatures and the tendency of the resulting NiS to melt (an endothermic process).

The least exothermic reaction is reaction **(18)**. As the temperature rises from 500 to 900 °C, the ΔH values for this reaction increase (become less negative), ranging from -254.005 to -170.986 kJ/mol, and then at 1000 °C they decrease sharply (become more negative) to -260.87 kJ/mol. This indicates a sharp change in the oxidation process at high temperatures, favouring the formation of the low-sulphur compound Ni_3S_2.

Based on the thermodynamic analysis, the relative probability of forming lower sulphides of various metals in the 500–1000 °C temperature range can be ordered as Fe > Ni > Co. This means iron sulphide (FeS) forms most readily. In contrast, formation of nickel (NiS) and cobalt (CoS) sulphides requires higher temperatures and lower partial pressures of sulphur and oxygen.

The ΔG vs. T diagrams (**Figs. 9, 10**) for reactions (1)–(18) (oxidation of iron, nickel, and cobalt sulphides in the 500–1000 °C range) show that most reactions are thermodynamically probable (ΔG < 0). The sequence of possible reactions during roasting depends on temperature and proceeds in order of increasing thermodynamic advantage, i.e., in the direction of more negative ΔG values. Increasing the temperature adversely affects the course of reactions 10 ($3CoS_{1.333} + O_2 \rightarrow 3CoS + SO_2$) and 12 ($CoS_{1.333} + 0.443\ O_2 \rightarrow CoS_{0.89} + 0.443\ SO_2$). At 1000 °C, their ΔG values become positive, indicating that these reactions are thermodynamically unfavourable and cannot proceed spontaneously.

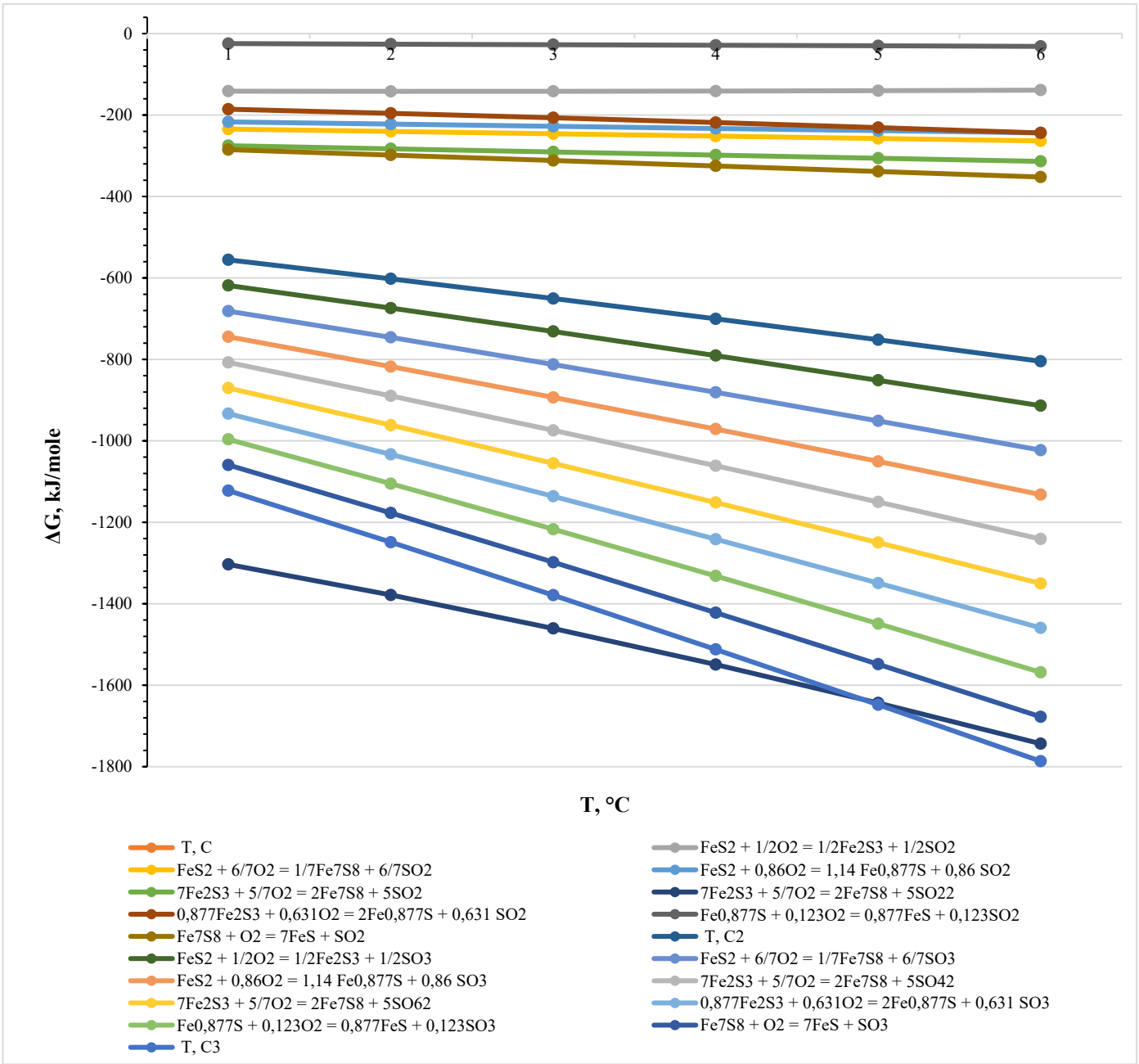

Fig. 9 Temperature dependence of ΔG for sulphide oxidation reactions

In this temperature range, during thermal activation of sulphides in an oxygen-deficient atmosphere, the formation of lower sulphides is thermodynamically possible in the following order (from most to least favourable): $Fe_7S_8 \rightarrow FeS \rightarrow Fe_7S_8 \rightarrow Fe_{0.877}S_8 \rightarrow Fe_2S_3 \rightarrow Fe_2S_3$; $Ni_3S_2 \rightarrow Ni_3S_4 \rightarrow NiS \rightarrow Ni_3S_2$; $CoS \rightarrow CoS_{0.89}$.

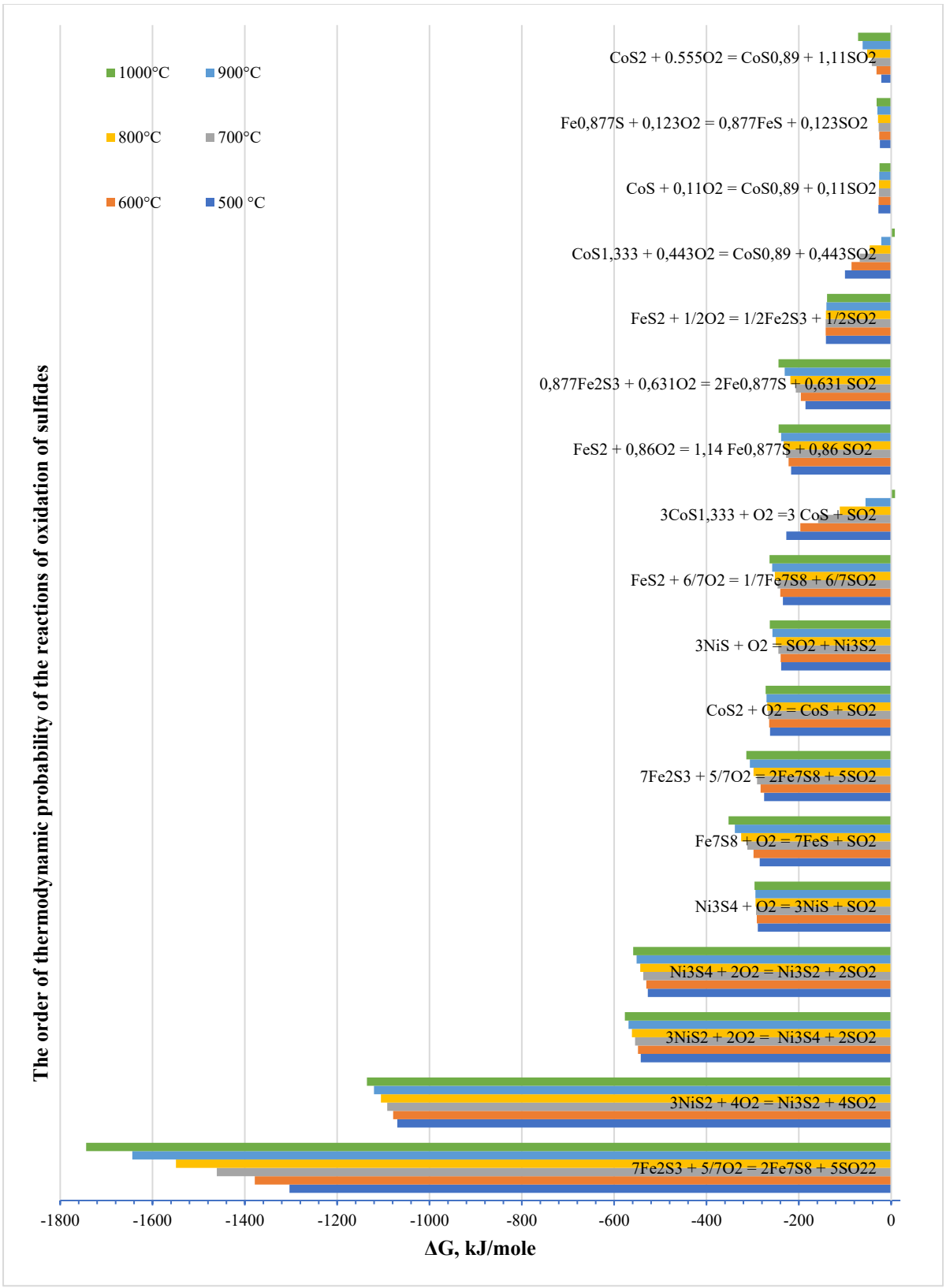

Fig. 10 Gibbs free energy vs. T for sulphide oxidation reactions. Partial pressure diagram of Fe–S–O, Ni-S-O and Co-S-O systems

Equilibrium partial pressure diagrams for the Fe–S–O, Ni–S–O, and Co–S–O systems were constructed to predict phase equilibria, determine thermodynamically stable phases, and establish the sequence of phase transformations during thermal decomposition of metal sulphides under oxygen-deficient conditions (**Fig. 11**).

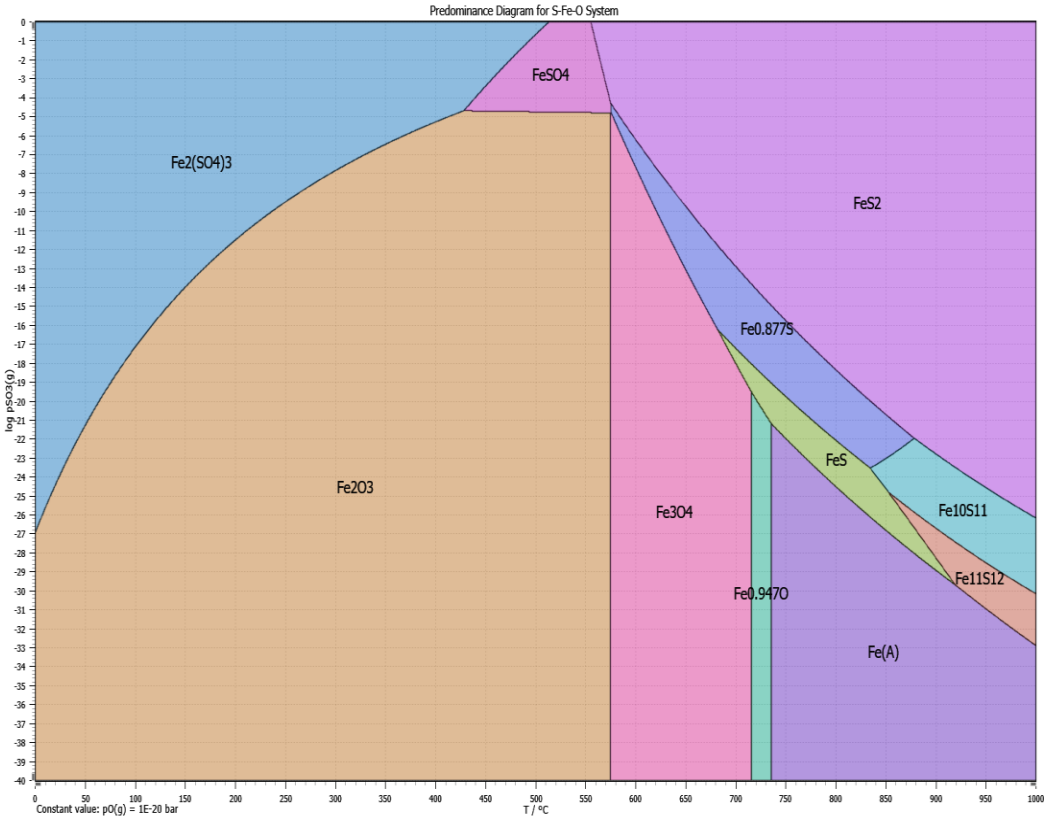

a)

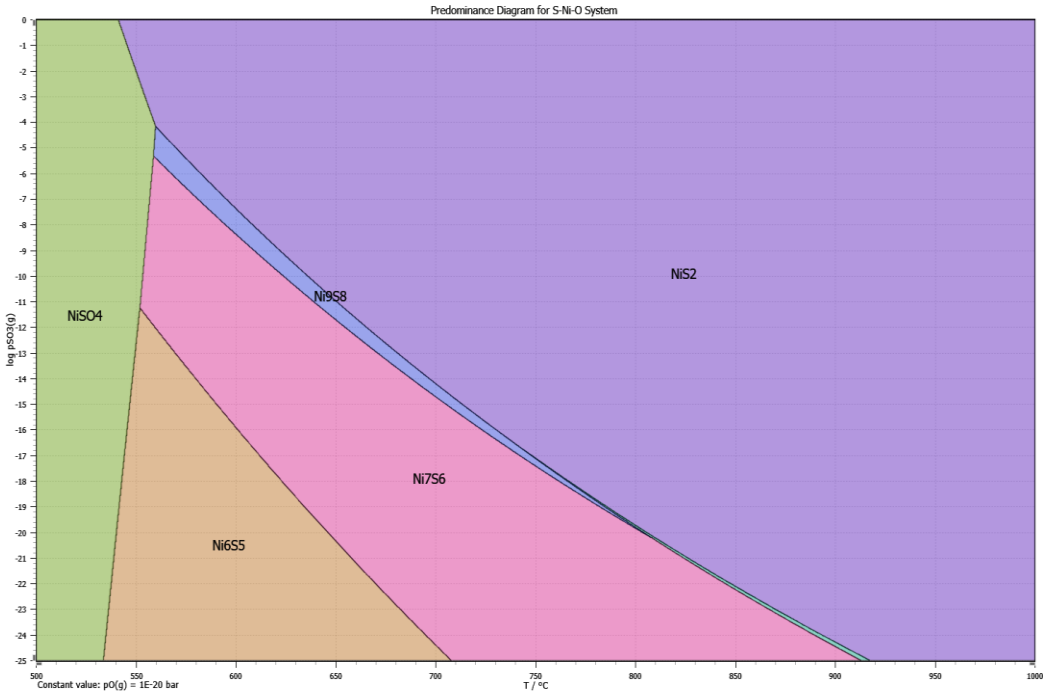

b)

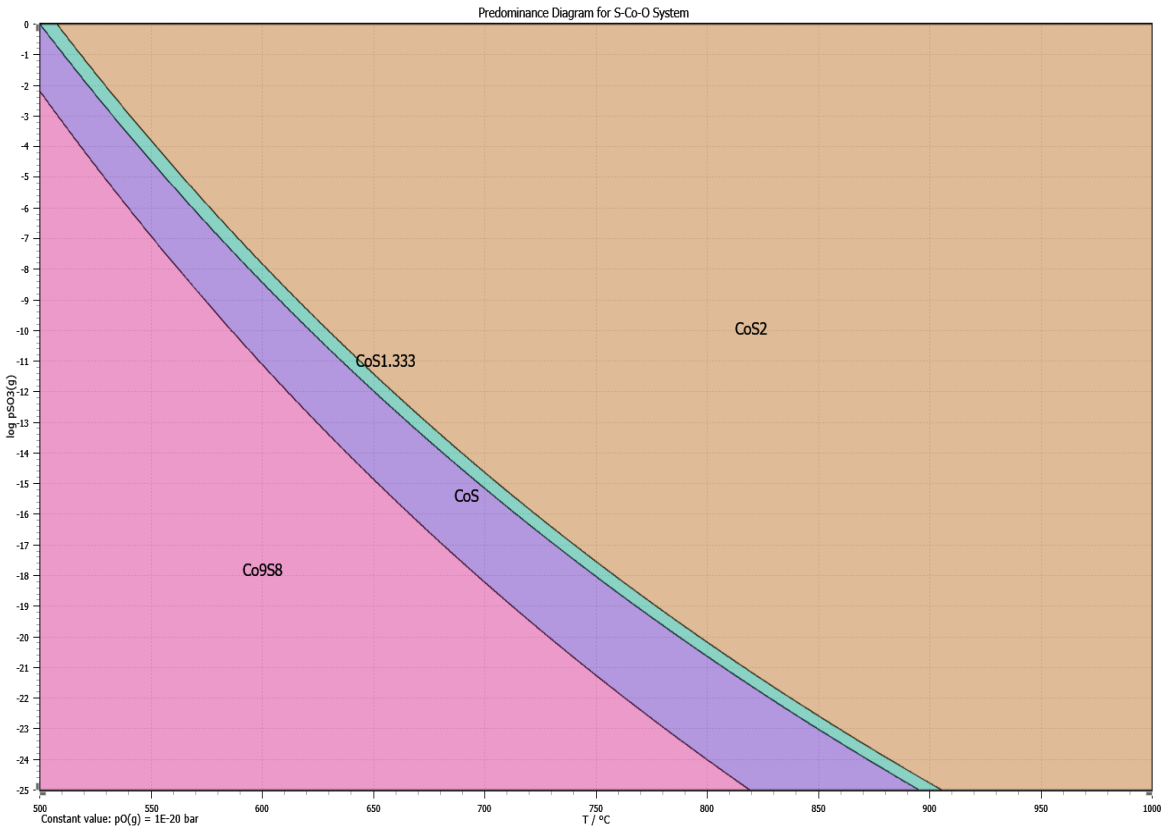

c)

Fig. 11 Diagrams of logp(SO_3)-f(T) dependencies for Fe-S-O (a), Co-S-O (b) and Fe-S-O (c) systems in the temperature range from 500 to 1000 °C

To obtain low-sulphur compounds in the Fe–S–O (**Fig. 11a**) system at a given partial oxygen pressure ($pO_2 = 10^{-20}$ bar), it is sufficient to reduce the partial pressure of sulphur trioxide p(SO_3) from –6 to –32 and increase the temperature to 600 °C and above. Such thermal activation conditions promote the decomposition of pyrite and the formation of a less sulphurous iron compound. The decomposition of pyrite occurs in stages, forming a series of non-stoichiometric pyrrhotites (Fe_2S_3, $Fe_{0.87}S$; general formula $Fe_{1-x}S$) which are characterised by variable composition, structural differences, and widely varying physical and chemical properties. A decrease in the partial pressure of sulphur dioxide p(SO_3) below –12 (at a given pO_2) leads to the formation of pyrite. Conversely, when temperature decreases and at higher concentrations of oxygen and sulphur dioxide, iron oxides (FeO, Fe_3O_4, Fe_2O_3) or sulphates ($FeSO_4$) are formed.

Analysis of the Ni–S–O diagram (Fig. 11b) shows that nickel disulphide becomes unstable when the partial pressure of sulphur dioxide p(SO_3) falls below about –4 and temperature is < 930 °C. Its decomposition proceeds through the formation of pentlandite (Ni_9S_8), stable between 400–610 °C. However, at temperatures above 610 °C, Ni_9S_8 reacts to form Ni_3S_2 and NiS, which is effective for our purposes. Depending on sulphur and oxygen pressures, the system may form nickel sulphides Ni_7S_6 and Ni_6S_5, which are also unstable; the final decomposition products are Ni_3S_2 and NiS via sequential reactions: $Ni_7S_6 \rightarrow Ni_6S_5 + NiS$ and $Ni_6S_5 \rightarrow Ni_3S_2 + 3NiS$. Thus, at temperatures above 600 °C under a partial SO_3 pressure of – 4 or lower, lower nickel sulphides form sequentially: $NiS_2 \rightarrow Ni_9S_8 \rightarrow Ni_7S_6 \rightarrow Ni_3S_2 \rightarrow NiS$.

In the Co–S–O system (Fig. 11c), p(SO_3) < 0 and a temperature of 600-900 °C are required for the formation of lower cobalt sulphides. When the SO_3 concentration in the gas phase decreases, thermal dissociation of cobalt disulphide occurs with sequential formation of lower cobalt sulphides: $CoS_2 \rightarrow CoS_{1.333} \rightarrow CoS \rightarrow CoS_{0.89}$. In the presence of cobalt pentlandite (Co_9S_8), decomposition proceeds via $Co_9S_8 \rightarrow Co_4S_3 + Co_{1-x}S$ (a non-stoichiometric phase close to CoS). Oxidation of nickel sulphide at temperatures above 600 °C under near-atmospheric SO_2 pressure proceeds sequentially through phases: $NiS_2 \rightarrow Ni_9S_8 \rightarrow Ni_7S_6 \rightarrow Ni_3S_2 \rightarrow NiS \rightarrow NiO \rightarrow NiSO_4$. At about 620 °C and near-atmospheric SO_2 partial pressure, cobalt oxidation proceeds via phases: $CoS_2 \rightarrow CoS_{1.333} \rightarrow CoS \rightarrow CoO \rightarrow CoSO_4$ [29].

Thermal analysis of pyrite concentrate

To determine the behaviour of the main sulphides in the nickel- and cobalt-containing pyrite concentrate during roasting, thermal analysis (TG) and differential scanning calorimetry (DSC) were carried out in the temperature range of 20–800 °C in an inert atmosphere (Fig. 12) at a heating rate of 10 °C/min.

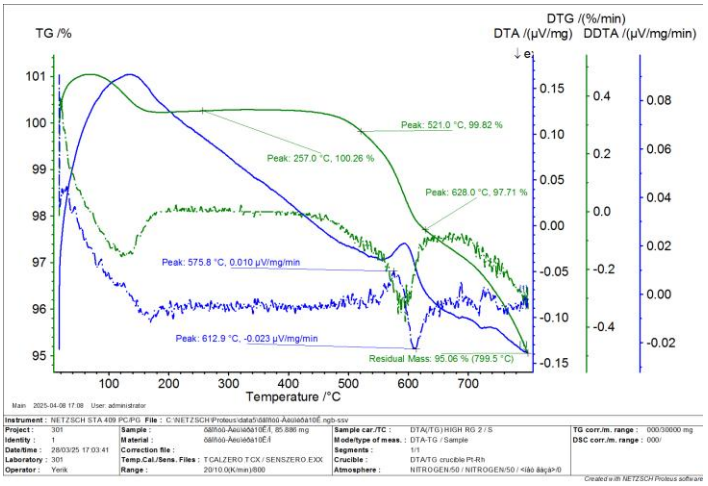

Fig. 12 Results of thermogravimetric analysis (TGA) and differential scanning calorimetry (DSC) of a pyrite sample in the temperature range of 20–800 °C in an inert environment

The thermogravimetric analysis results show that the TG, DTA, and DSC curves of the pyrite sample exhibit the following decomposition stages in the specified temperature intervals:

1) The first decomposition stage occurs in the 80–250 °C range. In this interval, the TG curve shows a 0.07% mass loss, and the DTA curve shows endothermic peaks at 140, 165, and 235.5 °C. These data indicate the loss of adsorbed and/or crystallisation water from sulphides and gangue minerals.

2) The second stage in the 300–700 °C range features both endothermic and exothermic effects: one exothermic effect at 566.6 °C (0.001 μV/mg/min), corresponding to the oxidation and/or decomposition of sulphides, and two endothermic effects with peaks at 600 and 614.1 °C (–0.000 μV/mg/min), which indicate the main decomposition of pyrite concentrate components—pyrite and nickel and cobalt sulphides—with the release of volatile products. In this interval, pyrite (FeS_2) begins to decompose, releasing sulphur and forming lower iron sulphides according to the reaction:

$$FeS_2 + O_2 = FeS + SO_2.$$

The resulting pyrrhotite (FeS) has greater solubility in acids than pyrite and is magnetic, allowing magnetic separation for extraction. At higher temperatures and with even more restricted oxygen, elemental sulphur may form:

$$FeS_2 = FeS + 0.5\ S_2\ (g).$$

In the presence of O_2, pyrite first undergoes partial desulphurisation with the formation of pyrrhotite and S_2, followed by slight oxidation of S_2. With a lack of oxygen, Fe_2S_3 and Fe_7S_8 may form. Additionally, when oxygen becomes available due to decomposition of gangue minerals, these sulphides are easily oxidised to FeS and SO_2. Increasing temperature leads to the formation of lower sulphides such as Fe_7S_8, $Fe_{0.877}S$, and Fe_2S_3 from pyrrhotite. In the presence of oxygen, these are easily oxidised to pyrrhotite ($Fe_{0.875}S \rightarrow FeS$). These data are consistent with results reported by other authors [30-32].

In the 500–700 °C range, reactions occur that form lower nickel sulphides Ni_3S_4 and Ni_3S_2. In the presence of oxygen, the resulting Ni_3S_4 transforms into millerite (NiS), and cobalt monosulphide may also form.

Within this temperature range, a total mass loss of 0.09–0.20% is observed (the sample retains 99.91–99.80% of its mass).

3) The third stage occurs in the 700–800 °C range. In this interval, exothermic peaks (at 720.6, 725, 740 °C, etc.) indicate oxidation processes of lower metal sulphides, phase transitions in the remaining and newly formed low-sulphur sulphides, or reactions between them (e.g., between iron sulphides and nickel-cobalt sulphides), leading to the formation of new phases.

According to studies by other authors [33], at temperatures above 700 °C, low-grade nickel sulphides $Ni_{3-x}S_2$ begin to decompose, and the immediate decomposition products are Ni_3S_2 and possibly Ni_7S_6. At ~797 °C, NiS starts to decompose, transitioning from a solid to a liquid state, and, as the temperature increases further, decomposes into metallic nickel and sulphur.

However, this temperature range favours the oxidation of cobalt monosulphide to $CoS_{0.89}$. Up to 747 °C, cobalt pentlandite (Co_9S_8) forms, but when temperature drops, it can transform into Co_3S_4.

With a further decrease in oxygen partial pressure, decomposition of nickel and cobalt sulphides proceeds to form sulphides poorer in sulphur or even to elemental metals, with the formation of elemental sulphur [34, 35].

Thus, at temperatures above 700 °C, partial oxidation of the remaining sulphides occurs via residual oxygen (released by the decomposition of some gangue metal oxides) and the transformation of lower sulphides. The mass loss in this stage is insignificant, amounting to only ~0.03%.

Kinetics and mechanism of pyrite concentrates decomposition

To determine the kinetics and mechanism of pyrite concentrate decomposition, thermal analysis experiments were performed on samples at heating rates of 10, 20, and 30 °C/min in a nitrogen atmosphere (**Fig. 13, 14**). The sensitivity of the weight measurement was 0.2 μg, with an error in weight loss determination of ±0.1%. The sensitivity of thermal effect measurement (peak positions on the DTA curve) was 0.06 μV.

Comparison of TG curves at 10, 20, and 30 °C/min (**Fig. 14**) shows that the sulfide decomposition reaction shifts to higher temperatures. Mass loss increases from 4.94% to 7.65%, indicating that the reaction has completed in the high-temperature areas.

The activation energy for the decomposition of pyrite concentrate in a nitrogen atmosphere was determined in the temperature ranges 450–479.3 °C, 661.8 °C, 749.7 °C, and 789 °C (**Fig. 14, Table 5**) using the Friedman method based on peak areas and degrees of conversion, with the Thermokinetics program.

Analysis of the activation energy values for the thermal decomposition stages indicates the multistage nature of the sample's decomposition. As temperature rises, each subsequent stage requires significantly higher activation energy, suggesting that more stable compounds enter into reaction-specifically, the decomposition of iron and cobalt sulphides requires more energy.

The relationship between the degree of conversion and time shows that the reaction rate during heat treatment is directly proportional to temperature-the higher the temperature, the faster the reaction proceeds.

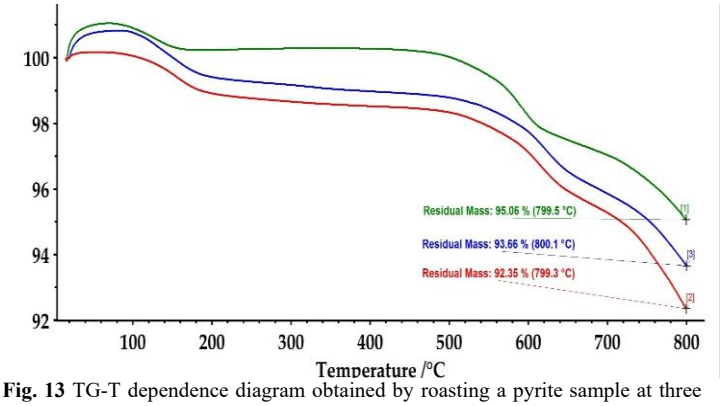

Fig. 13 TG-T dependence diagram obtained by roasting a pyrite sample at three heating rates (10, 20, and 30 °C per minute) in a nitrogen atmosphere.

Table 5 Activation energy values for thermal decomposition stages of pyrite concentrate

Temperature, °C	ΔG, kJ/mol	Stage
450-479,3 ºC	105-115 kJ/mol	I stage
661,8 ºC	310 – 320 kJ/mol	II stage
749,7 ºC,	390 – 400 kJ/mol	III stage
789 ºC	420 kJ/mol	III stage

The change in kinetic parameters during the reaction confirms that the process involves several parallel or sequential stages with different activation energies.

Analysis of the kinetic plot [α(%) -f(τ)] (**Fig. 15**) across the 610–680 °C temperature range demonstrates that the decomposition process rate is strongly temperature-dependent. For each isotherm, the reaction rate is maximal at the initial stage (τ~0) and progressively decreases as the pyrite sample is consumed. Elevating the temperature significantly intensifies the process: at 610 °C (the lowest curve), the reaction is barely initiated (α~2-3%), whereas at 680 °C (the uppermost curve), it does not reach full completion within 7 minutes, reaching α~80%.

The observed changes in kinetic parameters during the reaction confirm that the process involves several parallel or sequential stages with distinct activation energies.

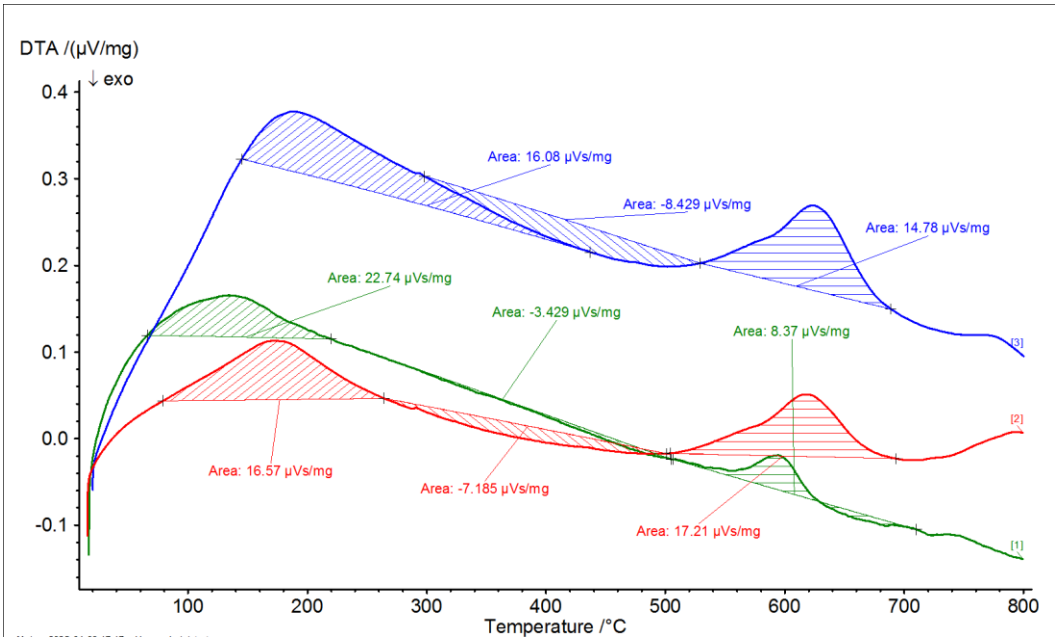

Fig. 14 DTA-f(T) diagram obtained by roasting a pyrite sample at three heating rates (10, 20, and 30 °C per minute) in a nitrogen atmosphere

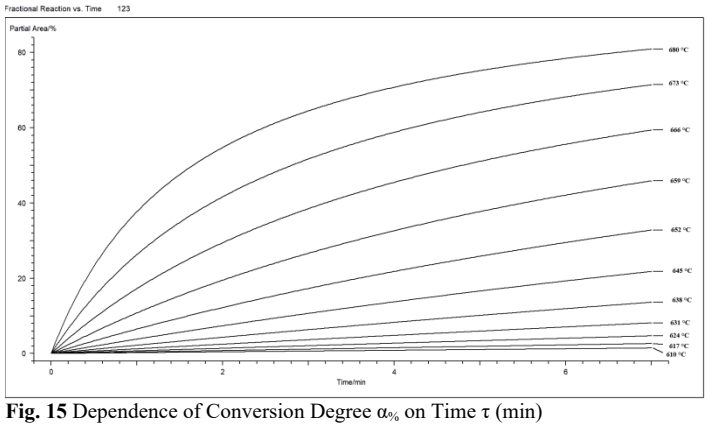

Fig. 15 Dependence of Conversion Degree $\alpha_{\%}$ on Time τ (min)

The change in log A (pre-exponential factor) for 10 °C/min from –29 to –9.5, for a heating rate of 20 °C/min from –30 to –12.5, and for 30 °C/min from –31.0 to –12.5, indicates a change in the mechanism of pyrite concentrate decomposition reactions (Fig. 16).

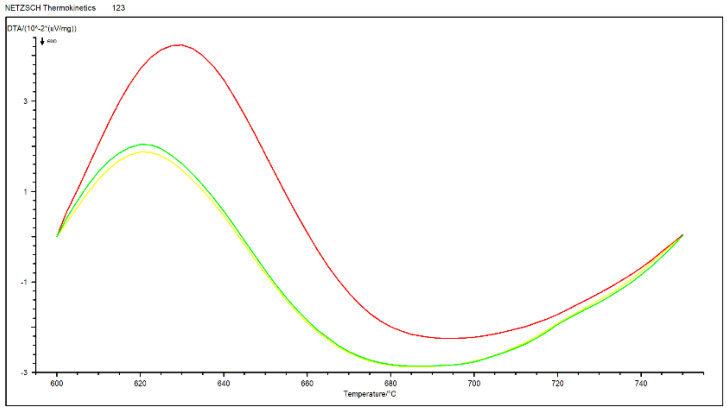

Fig. 16 Dependence of activation energy E and log(A/s^{-1}) on conversion α (isoconversional analysis by Friedman's method)

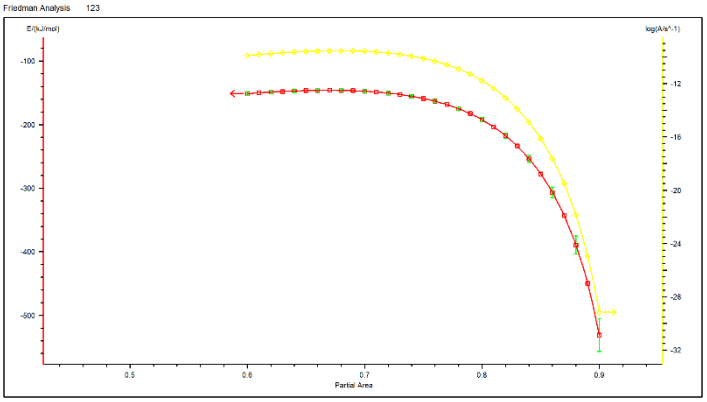

Fig. 17 DTA curves of pyrite concentrate thermal decomposition at heating rates of 10, 20, and 30 °C/min

The DTA–f(T) graph (**Fig. 17**) indicates that pyrite concentrate decomposition in the 600–740 K range proceeds in two stages with an exothermic effect followed by an endothermic effect, and the heating rate significantly affects the temperature and kinetics of decomposition. Positive peaks on the curves indicate oxidation of pyrite, nickel, and cobalt sulphides in an oxygen-containing atmosphere. As the heating rate increases, the decomposition temperature rises; at higher heating rates, the decomposition process requires more energy, consistent with the calculated activation energies.

Thus, the process of roasting pyrite concentrates under limited oxygen supply functions as an activational roast for refractory sulfides. This methodology offers significant energetic and economic advantages due to the inherently exothermic nature of the reactions, resulting in reduced energy and time consumption. Crucially, this controlled environment promotes the preferential formation of acid-soluble, non-stoichiometric lower sulfides of iron, nickel, and cobalt. Simultaneously, sulfur dioxide (SO2) is liberated, serving as the primary raw material for downstream sulfuric acid production, thereby enhancing the overall technological and economic viability of the process.

Based on complex thermodynamic and thermal analyses and the observed kinetics of sulfide oxidation reactions under oxygen-limited conditions, it is concluded that pyrite concentrate decomposes effectively within the temperature range of 300-700 °C; however, higher temperatures primarily drive interphase transformations

of the sulfides and subsequent oxidation. The resulting residue containing low-grade sulfides is recommended for sulfuric acid leaching.

Roasting results

Pyrite concentrates were roasted using the above method at a temperature range 600–700 °C. The resulting cinders are characterised by low sulphur content, which decreased from 5.50% to 3.00% (**Table 6)**.

Table 6 Chemical composition of cinders obtained at 600–700 °C (wt. %)

Content, %						
T,°C	Fe	Cu	Co	Ni	S	Pb
600	16,24	0,031	0,017	0,017	3,6-3,8	0,0023
	Zn	SiO_2	Al_2O_3	CaO	MgO	TiO_2
	0,041	34,63	13,51	11,32	3,45	0,65
700	Fe	Cu	Co	Ni	S	Pb
	17,02	0,036	0,021	0,022	3,0-3,45	0,0023
	Zn	SiO_2	Al_2O_3	CaO	MgO	TiO_2
	0,042	34,64	13,62	11,34	3,75	0.66

SEM-EDS analysis **(Fig. 18**) shows that roasting at 600–700 °C results in significant changes in the material's chemical composition and phase structure. The raw concentrate (**Fig. 18a**) contains high Fe and S, along with impurities of Al, Si, Ca, Ti, and Mg originally present in the crystal lattice or as inclusions. Roasting at 600 °C (**Fig. 18b**) causes marked changes: increased surface porosity and extensive desulphurization of pyrite (as evidenced by a decrease in sulphur content and an increase in iron content), as well as partial oxidation of pyrite to iron oxides. The concentrations of Ni, Co, and Cu at the calcine surface increase (relative to the raw concentrate), and As is almost completely removed (**Fig. 18c**) and **Table 6**. These effects are due to the destruction of the pyrite matrix during roasting, which releases nickel, cobalt, copper, and other metals.

Leaching results

Leaching studies on the thermally activated pyrite samples were conducted in glass flasks fitted with reflux condensers and stirrers. The stirring speed was kept constant in all experiments.

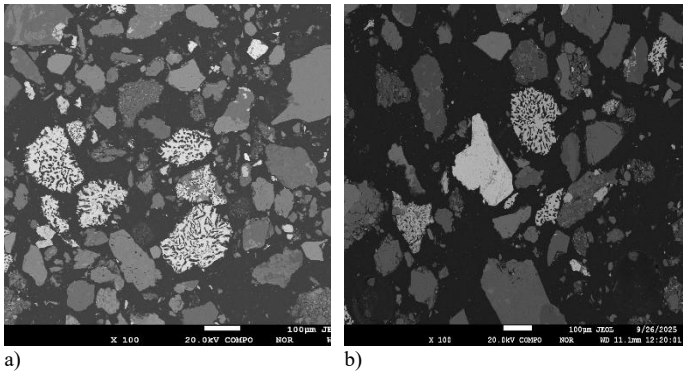

a) b)

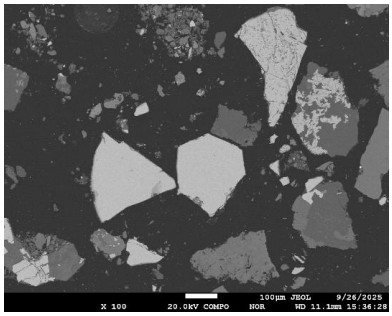

c)

Fig. 18 SEM images at ~100× magnification and EDS spectra of a) raw pyrite, b) pyrite calcined at 600 °C, c) pyrite calcined at 700 °C

Effect of roasting temperature

Leaching tests were performed on concentrates roasted at 600 °C, 650 °C, and 700 °C. The results (**Fig. 19**) show that as the roasting temperature increases from 600 to 700 °C, the extraction of all metals improves. Iron is largely extracted at all roasting temperatures. The nickel extraction into solution increases by about 22%, reaching ~ 93.2% when leaching the calcine obtained at 700 °C. The dissolution of cobalt increases almost linearly with roasting temperature: the Co extraction approximately doubles, from 46.3% to 91.3%, as the roasting temperature rises from 600 °C to 700 °C. The correlation equations and the high regression coefficient (R ≈ 1) indicate that the chosen calcination conditions are appropriate. A roasting temperature of 700 °C is favorable for maximum extraction.

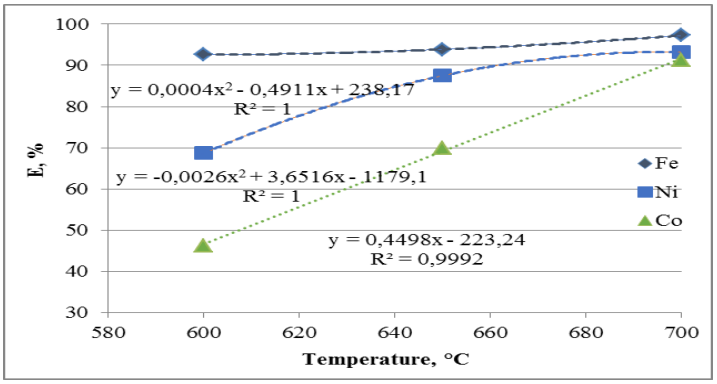

Fig. 19 Effect of roasting temperature on metal extraction

Effect of sulfuric acid concentration

The influence of acid concentration was evaluated by varying the acid-to-solid ratio (stoichiometric excess, R) from 0.52 to 2.0. The results (**Fig. 20**) show that increasing the acid amount leads to higher extraction of all metals. Iron extraction is high even at the lower acid amounts: raising R from 0.5 to 1.5 increases Fe extraction from 67.1% to 94.0%, and further increasing R to 2.5 yields 97.9%. The extraction of nickel into solution rises from 58.1% to 95.9% as R is increased from 0.5 to 2.5. No cobalt is leached at R = 0.5; with R raised to 1.5, the Co extraction reaches 93.0%, and a further increase to R = 2.5 does not significantly improve it. Therefore, an R value of 1.5 was selected as optimal for acid consumption.

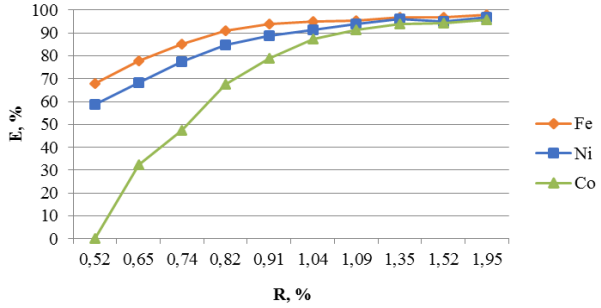

Fig. 20 Effect of sulphuric acid excess R on metal extraction

Effect of leaching duration

Leaching kinetics were investigated by varying the leaching time from 5 to 240 minutes, while keeping the acid amount at R = 1.5, the roast at 700 °C, and the leaching temperature at 100 °C. The results are summarised in **Fig. 21**. All three target metals (Fe, Ni, Co) show increasing extraction with longer leaching time, but their behaviours differ somewhat.

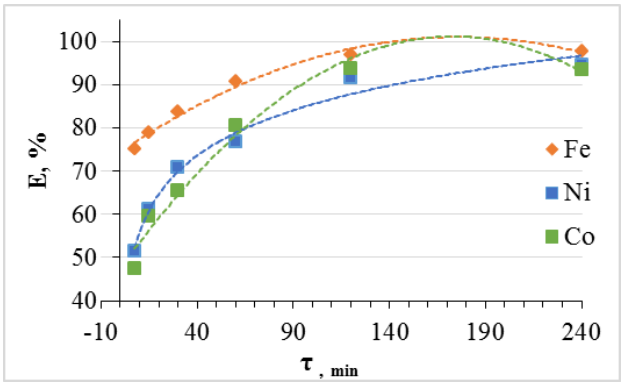

Fig. 21 Effect of leaching duration on metal extraction

Iron is extracted very rapidly. The Fe extraction after just 5 minutes was already in the 60–70% range. It then gradually increased to ~94% by 120 minutes, and further time up to 240 minutes did not significantly change the Fe recovery.
Nickel shows a sharper dependence on time, especially in the initial period. In the first 30 minutes, Ni extraction increased steeply—from ~0% at 5 min to ~50–60% at 30 min. After 120 minutes, Ni extraction reached ~93%, and then plateaued. The curve suggests a saturation effect.
Cobalt also increases with time, but in a more nonlinear pattern. Initially, for up to ~30 min, Co extraction rises relatively quickly—from 0 to ~30–40% —then the rate of increase tapers off. Co often leaches faster than Ni initially because some Co might form soluble sulphates. Co extraction ~93% by 120 minutes similar to Ni extraction rate. Beyond 2 hours, there is an indication that the Co extraction might peak and even begin to decline slightly. However, over the tested duration, Co essentially plateaued at a recovery level similar to that of Ni.
From these observations, it is concluded that a leaching duration of 120 minutes is sufficient to achieve >90% recovery of Ni, Co, and Fe. Longer durations up to 4 hours did not significantly improve yields and are therefore unnecessary for practical purposes.
The slight differences in the time-dependence reflect the leaching mechanisms - iron, mostly present as soluble phases after roasting (FeS or $FeSO_4$), dissolves fastest, while nickel and cobalt derived from sulphides take longer.
The order of extraction rates initially was Fe > Co > Ni. But finally, all approaches are similar in their extent.

Effect of temperature

The influence of leaching temperature on target metal extraction was studied at temperatures ranging from room temperature (20 °C) to 120 °C, with a fixed acid excess (R = 1.50) and a leaching time of 2 hours. The results (**Fig. 22**) show a very strong positive effect of temperature on the leaching efficiency:

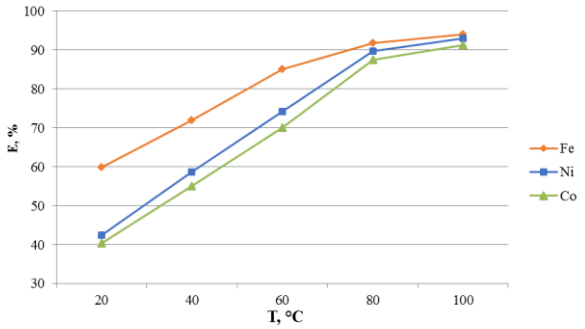

Fig. 22 Effect of temperature on metal extraction

At 20 °C, the extractions were very low, indicating that ambient-temperature leaching of the roasted concentrate is ineffective within 2 hours. As the temperature increased from 60°C to 80°C, then to 100 °C, there were steep increases in the dissolution of all metals. By 100 °C, iron extraction reached 94.4%, cobalt 91.2%, and nickel 93.1%. There was only a barely useful further increase when going to the range 110–120 °C. Essentially, near-complete leaching of all three metals requires temperatures close to the boiling point of the acid. This is typical for a process where the leaching rate increases exponentially with increasing temperature (Arrhenius behavior).
Ultimately, at ≥100 °C all three metals were leached to roughly the same high level – more than 90%. Therefore, 100–110 °C is recommended as the operating leaching temperature for practical purposes, as it achieves high recoveries without the need for specialized high-pressure equipment.
The experimental data across various leaching conditions of samples (roasting temperature, sulfuric acid concentration, leaching duration and temperature) were used to derive empirical models correlating the extraction degree (E, %) of each main metal (Fe, Co, Ni) with these factors. Table 7 illustrated the polynomial regression equations and their R^2 values, and it can be used to predict the extraction outcomes within the studied parameter ranges. All models have very high quantity of R^2 (0.97–0.99), reflecting an excellent fit.

Table 7 Quadratic model equations and R^2 for metal extraction as functions of leaching parameters

	Factors	Me extraction model equation	Approximation coefficient, R^2
1	**Temperature, 20-120 °C**		
	Fe	$y = -1{,}8514x^2 + 19{,}927x + 41{,}138$	0,9947
	Ni	$y = -1{,}8293x^2 + 24{,}193x + 19{,}138$	0,9911
	Co	$y = -1{,}3871x^2 + 21{,}745x + 18{,}9$	0,9868
2	**Acid concentration, excess coefficient R 0.5–2.0**		
	Fe	$y = -0.5813x^2 + 9{,}9275x + 61{,}106$	0,9737
	Ni	$y = -0.6372x^2 + 10{,}961x + 49{,}338$	0,9923
	Co	$y = -1{,}7293x^2 + 28{,}767x – 22{,}709$	0,9914
3	**Duration of leaching, 5–240 min**		
	Fe	$y = -0{,}0009x^2 + 0{,}303x + 74{,}427$	0,9835
	Ni	$y = -0{,}0014x^2 + 0{,}5025x + 52{,}315$	0,9659
	Co	$y = -0{,}0014x^2 + 0{,}5025x + 52{,}315$	0,9659

The models confirm the trends described: a quadratic dependence on temperature, a similarly strong effect of acid with diminishing returns at high R, and a time dependence that levels off. These equations are useful for process optimisation and scale-up calculations.
Conditions for single-stage leaching of pyrite-cobalt concentrate were determined to be: temperature 100–110 °C; duration 2 hours; solvent excess R=1.5. After leaching, the solutions contained approximately 160–162 g/dm³ Fe, 0.238 g/dm³ Co, and 0.223 g/dm³ Ni. To reduce acid consumption, countercurrent continuous leaching can be performed.

Balance experiments on leaching raw and thermally activated concentrates

Finally, balance-leaching experiments were conducted to compare overall metal recovery from raw versus thermally activated material. In these tests, 100 g samples of raw pyrite concentrate and of the roasted concentrate (700 °C, 1 h) were leached under the same optimal conditions: T = 100 °C, R = 1.5, 2 h. The approximate leaching mass balance is given in **Table 8**.

Table 8 Leaching mass balance comparison for raw vs. thermally activated pyrite concentrate

Materials	**Extraction, %**			**Products obtained**	**Extraction, %**		
	Fe	Ni	Co		Fe	Ni	Co
Raw pyrite concentrate	34,25 %	5,75	-	Thermally activated concentrate	94,03	93,01	91,49

These results underscore the critical importance of the roasting step. Thermal activation improved iron recovery by about a factor of 3 (from 34% to 94%) and nickel and cobalt recovery by well over an order of magnitude (from near-zero to over 90%). Direct leaching of pyrite tailings without roasting would only recover iron, with nickel and cobalt largely unrecovered, whereas the combined roasting–leaching approach efficiently recovers all three metals.
On an operational note, after leaching the roasted concentrate, the resulting slurry settled and filtered easily. The leachate solutions are rich in Fe and contain Ni and Co, and are suitable for further purification by solvent extraction or precipitation

to produce metal salts. The residual solids after leaching of sinders are mostly inert and volume-reduced relative to the original tailings.

The proposed combined technology thus transforms pyrite tailings into a new resource: it allows the extraction of valuable residual metals (Ni, Co, Fe). It captures sulphur as SO_2 (which is used to produce H_2SO_4 for the process itself or other uses). This effectively closes the loop of iron ore processing, converting a linear flow into a circular economy model [37]. [36].

CONCLUSION

A nickel–cobalt-bearing pyrite concentrate, sourced from the SSGPO plant, contains approximately 15.8% iron (Fe), 0.012% nickel (Ni), 0.013% cobalt (Co), and about 5.5% sulfur (S). The primary mineral in this concentrate is pyrite, while the gangue is comprised of silicates such as quartz, analcime, albite, and amphibole (tremolite).

A combined processing method has been developed for this raw material, which includes thermal activation in an oxygen-limited atmosphere followed by leaching with sulfuric acid. The purpose of thermal activation is to convert the nickel and cobalt sulfides into lower sulfide forms that are more amenable to leaching.

Thermodynamic analyses suggest that the thermal decomposition of the pyrite concentrate occurs through a multi-stage process, primarily driven by exothermic oxidation reactions. Within a temperature range of 500–1000 °C and under limited oxygen conditions, lower metal sulfides form in the following order of ease: FeS > NiS > CoS.

Thermogravimetric (TG) and differential thermal analysis (DTA) data indicate that the main thermal decomposition of higher sulfides is initiated and largely completes between 300 and 700 °C. Optimal conversion of nickel and cobalt to the lower sulfides occurs at temperatures between 600 and 700 °C. Kinetic studies show that increasing the thermal activation temperature accelerates sulfide dissociation, consistent with the higher apparent activation energy observed at higher reaction temperatures.

Above 700 °C, exothermic processes, primarily involving phase transformations and the oxidation of lower sulfides, become predominant.

During roasting at around 600-700 °C, the sulfur content of the pyrite concentrate is reduced by approximately 40–45%. Under optimal leaching conditions for the activated concentrate, the recovery rates of metals into solution are as follows: 94.03% for iron (Fe), 93.01% for nickel (Ni), and 91.49% for cobalt (Co).

In conclusion, the developed combined technology of thermal activation followed by leaching presents an effective and viable method for the high-yield recovery of nickel and cobalt from refractory pyrite waste.

Acknowledgements: This research was funded by the Science Committee of the Ministry of Science and Higher Education of the Republic of Kazakhstan (Grant No. AP19680477).

REFERENCES

1. T. Norgate, S. Jahanshahi: Minerals Engineering, 23, 2009, 65-73. https://doi.org/10.1016/j.mineng.2009.10.002
2. P. Edgar, B. Arthur, T. Asim: Minerals Engineering, 24(7), 2011, 625-637. https://doi.org/10.1016/j.mineng.2010.10.004
3. D.W. Blowes, et al.: The Geochemistry of Acid Mine Drainage, *Treatise on Geochemistry*, Elsevier Science, 2014, 131-190. https://doi.org/10.1016/B978-0-08-095975-7.00905-0
4. M. B. Lindsay, M. C. Moncur, J. G. Bain, J. L. Jambor, C. J. Ptacek, D. W. Blowes: Applied Geochemistry, 57, 2015, 157-177. https://doi.org/10.1016/j.apgeochem.2015.01.009
5. E. Peters: Metallurgical and Materials Transactions B, 7, 1976, 505–517. https://doi.org/10.1007/BF02698582
6. W. Luo, Q. Feng, L. Ou, G. Zhang, Y. Chen: Minerals Engineering, 23(6), 2010, 458-462. https://doi.org/10.1016/j.mineng.2009.10.006
7. L. Xuheng, H. Jiahao, Z. Zhongwei, C. Xingyu, L. Jiangtao, H. Lihua: Hydrometallurgy, 215, 2023. https://doi.org/10.1016/j.hydromet.2022.105987
8. T. Ingraham, H. Parsons, L. Cabri: Canadian Metallurgical Quaterly. 11, 1972, 407–411. https://doi.org/10.1179/000844372795257575
9. N. Faris, M. I. Pownceby, W. J. Bruckard, M. Chen: Mineral Processing and Extractive Metallurgy Review, 44(6), 2023, 407-435. https://doi.org/10.1080/08827508.2022.2070617
10. D. J. Droppert, Y. Shang: Hydrometallurgy, 39(1-3), 1995, 169-182. https://doi.org/10.1016/0304-386X(95)00034-E
11. Y. Xie, Y. Xu, L. Yan, R. Yang: Hydrometallurgy, 80(1-2), 2005, 54-58. https://doi.org/10.1016/j.hydromet.2005.07.005
12. O. Elsayed, D. Zixian, L. Huan, E. Jacques, Minerals Engineering, 204, 2023. https://doi.org/10.1016/j.mineng.2023.108418
13. E. Oraby, Z. Deng, H. Li, J. Eksteen: Minerals Engineering, 204, 108418, 2023. https://doi.org/10.1016/j.mineng.2023.108418
14. B. Yaylali, H. Deveci, E. Y. Yazici, O. Celep: Minerals Engineering, 198, 2023, 108077. https://doi.org/10.1016/j.mineng.2023.108077
15. A. Karppinen, S. Seisko, M. Lundstrom: Minerals Engeneering 207, 108576, 2024. https://doi.org/10.1016/j.mineng.2024.108576
16. I. Perederiy, V. G. Papangelakis, M. Buarzaiga, I. Mihaylov: Journal of Hazardous Materials, 194, 2011, 399-406. https://doi.org/10.1016/j.jhazmat.2011.08.012
17. C. Joulian, A. Hubau, D. Pino-Herrera, A. G. Guezennec: Research in Microbiology, 175(1-2), 2024, 104112. https://doi.org/10.1016/j.hydromet.2023.108213
18. A. Ahmadi, M. Khezri, A. A. Abdollahzadeh, M. Askari: Hydrometallurgy, 154, 2015, 1-8. https://doi.org/10.1016/j.hydromet.2015.03.006
19. E. R. Ngoma, E. Cameron, J. A. Pakostova, T. A. Wiesner, N. Clark, Mykytczuk: Progress and Challenges in Pilot Bioleaching of Ni/Co from Sudbury Pyrrhotite-rich Mine Tailings*: The CanmetMINING Process*. In Conference of Metallurgists, 2024, 1131-1134. https://doi.org/10.1007/978-3-031-67398-6_192
20. G. Khodadadmahmoudi, et al.: Journal of Environmental Management, 317, 115394, 2022. https://doi.org/10.1016/j.jenvman.2022.115394
21. Y. Thibault, J. G. McEvoy, S. Beauchemin: Minerals Engineering, 150, 106265, 2020. https://doi.org/10.1016/j.mineng.2020.106394
22. G. Rui, W. Le. Transactions of Nonferrous Metals Society of China, 34(3), 2024, 1003-1015. https://doi.org/10.1016/S1003-6326(23)66449-0
23. T. Xiao, et al.: Minerals Engineering, 174, 107254, 2021. https://doi.org/10.1016/j.mineng.2021.107254
24. F. Cui, et al.: Minerals Engineering, 123, 2018, 104-116. https://doi.org/10.1016/j.mineng.2018.04.013
25. E. A. Mends, S. E. Arthur, S. Hussaini, J. S. Thella, P. Chu: Minerals Engineering, 231, 109433, 2025. https://doi.org/10.1016/j.mineng.2025.109433
26. Y. Merkibaev, V. Panayotova, V. Luganov, T. Panayotov, T. Chepushtanova: Comptes rendus de l'Acad´emie bulgare des Sciences. 71(8), 2018, 1116-1123. https://doi.org/10.1016/j.mineng.2025.109433
27. N.S. Ivanov, M.S. Malimbayev, A.Z. Abilmagzhanov, O.S. Kholkin, I.Ye. Adelbayev: Minerals Engineering, 18115, 2022. https://doi.org/10.1016/j.mineng.2022.107498
28. W. Yongwei, C. Xuejie, C. Mengjun, Q. Wenqing, H. Junwei: Minerals Engineering, 203, 2023. https://doi.org/10.1016/j.mineng.2023.108336
29. K. K. Mamyrbayeva, A.N. Kuandykova, T. A. Chepushtanova:. International Multidisciplinary Scientific GeoConference: SGEM, 4(2), 2024, 151-158. https://doi.org/10.5593/sgem2024v/4.2/s17.22
30. Y. Zhang, Q. Li, X. Liu, B. Xu, Y. Yang, T. Jiang: Minerals, 9(4), 2019, 220. https://doi.org/10.3390/min9040220
31. A.W. Coats et al.: Can. J. Chem. 1966. https://doi.org/10.1139/v66-176
32. N. Boyabat, A. K. Özer, S. Bayrakçeken, M. Ş. Gülaboğlu: Fuel processing technology, 85(2-3), 2004, 179-188. https://doi.org/10.1016/S0378-3820(03)00196-6
33. Wang, H: Journal of Sulfur Chemistry, 26(3), 2005, 233–243. https://doi.org/10.1080/17415990500195172
34. N. Kumar, N. Raman, A. Sundaresan: Zeitschrift für anorganische und allgemeine Chemie, 640(6), 2014, 1069-1074. https://doi.org/10.1002/zaac.201300649
35. P. H. Edwards, J. R. Bairan Espano, J. E. Macdonald: Chemistry of Materials, 36(15), 2024, 7186-7196. https://doi.org/10.1021/acs.chemmater.4c00911
36. T.A., Chepushtanova, K.K., Mamyrbaeva, V.A., Luganov, B. Mishra: Minerals and Metallurgical Processing. 29, 2012, 159-164. https://doi.org/10.1007/BF03402254